Provenance of the Greater Himalayan Sequence and associated rocks: Predictions of channel flow models

R.A. JAMIESON[1], C. BEAUMONT[2], M.H. NGUYEN[1,2] & D. GRUJIC[1]
[1]*Department of Earth Sciences, Dalhousie University, Halifax, N.S., Canada, B3H 3J5*
[2]*Department of Oceanography, Dalhousie University, Halifax, N.S., Canada, B3H 4J1*

Abstract: Numerical models for channel flow in the Himalayan-Tibetan system are compatible with many tectonic and metamorphic features of the orogen. Here we compare the provenance of crustal material in two channel flow models (HT1 and HT111) with observations from the Himalaya and southern Tibet. After 54 million years, the entire model crust south of the suture consists of "Indian" material. The model Greater Himalayan Sequence ("GHS") is derived from Indian middle crust originating ≤ 1000 km south of the suture, whereas the Lesser Himalayan Sequence ("LHS") is derived mainly from crust originating ≥ 1400 km south of the suture. Material tracking indicates little or no mixing of diverse crustal elements in the exhumed model "GHS". These results are compatible with provenance data indicating a clear distinction between GHS and LHS protoliths, with the GHS originating from a more distal position (relative to cratonic India) than the LHS. In model HT111, domes formed between the suture and the orogenic front are cored by "Indian" middle crust similar to the "GHS", consistent with data from the north Himalayan gneiss domes. Material tracking shows that plutons generated south of the suture should have "Indian" crustal signatures, also compatible with observations. Model "GHS" P-T-t paths pass through the dehydration melting field between 30 and 15 Ma, consistent with observed leucogranite ages. Finally, exposure of mid-crustal "GHS" and "LHS" material at the model erosion front is consistent with the observed appearance of sedimentary detritus in the Lesser Himalaya. We conclude that channel flow model results are compatible with provenance data from the Himalaya and southern Tibet.

Submitted to Geological Society of London Special Publication, Channel Flow Conference, December 2004

Numerical models for channel flow in the Himalayan-Tibetan system (e.g., Beaumont *et al.* 2001) predict that low-viscosity middle crust has flowed outward from beneath the Tibetan plateau, and has been exhumed between the Main Central Thrust zone (MCT) and South Tibetan Detachment system (STD) in response to focused denudation at the erosion front. Model results are compatible with a number of first-order tectonic and metamorphic features of the orogen (Beaumont *et al.* 2001, 2004; Jamieson *et al.* 2004). However, previous work did not address in detail the distribution of material from different sources within the model orogen. Material tracking in the models can be used to predict the provenance of rocks now exposed in the Greater Himalayan (GHS) and Lesser Himalayan (LHS) sequences and the north Himalayan gneiss domes, as well as the likely sources of Miocene leucogranites throughout the region. Conversely, provenance data from the orogen provide an important test of the models and additional constraints on material flow patterns within the model orogen. Here we present results from two channel flow models (HT1 and HT111) that display contrasting tectonic styles between the suture and the orogenic front. The purpose of this paper is to compare the distribution of crustal material at and below the model surfaces with provenance data from metamorphic, plutonic, and sedimentary rocks in the Himalaya and southern Tibetan.

In order to facilitate comparison between model results and data from the Himalayan-Tibetan orogen, the following nomenclature has been adopted in this paper. Model times are given in Ma, meaning "millions of years before the end of the model", equivalent to "millions of years before present" in nature. Model features appear in quotation marks; corresponding features of the real Himalayan-Tibetan system do not. The pro-side of the model is referred to as "India" (south) and the retro-side of the model is referred to as "Asia" (north). The upper crust above the model orogen is referred to as "Tethyan" material. The protolith boundary between incoming pro-crust and the outflowing channel is referred to as the "MCT", and the boundary between the extruded channel and the overlying upper crust is referred to as the "STD" (Jamieson *et al.* 2004). The initial boundary between pro-side and retro-side crust, interpreted to be equivalent to the Indus-Tsangpo suture zone, is referred to simply as the suture. The terms "distal" and "proximal" refer to relative distance from the pro-ward end of the model ("cratonic India") - pro-side distal material originates closer to the model suture than proximal material.

Model design

Models HT1 and HT111 (Fig. 1; Table 1) were selected from a series of related models (e.g., Beaumont *et al.* 2001, 2004) that illustrate features relevant to the Himalayan-Tibetan system. The design of model HT1 and its thermal-mechanical evolution were discussed in detail by Beaumont *et al.* (2004) and Jamieson *et al.* (2004). Model HT111 is identical to HT1 except that the upper crust contains an embedded weak layer; as detailed below, the weaker upper crust has a significant effect on model evolution. The numerical formulation and calculation procedure have been decribed elsewhere (Fullsack 1995; Beaumont *et al.* 2004, this volume).

Both models were run for 54 million years, with the convergence velocity, V_P = 5 cm/y, partitioned between S-point (subduction) advance at V_S = 2.5 cm/y and subduction at V_P-V_S = 2.5 cm/y (Fig. 1; Beaumont *et al.* 2004). The lower, middle, and upper crustal layers (Fig.1, Table 1) are laterally homogeneous. In model HT1, the upper crustal layer (0-10 km) has a wet quartzite (*B*(WQ)*) rheology (Gleason & Tullis 1995; details in Table 1) with an effective internal angle of friction, ϕ_{eff} = 5°. In model HT111, a *B*(WQ)* layer with ϕ_{eff} = 2° has been embedded in the upper crust between 4.5 and 7.0 km (Fig. 1). In both models, the rheology of the middle crustal

layer (10-25 km) is equivalent to *B*(WQx5)* with ϕ_{eff} = 15° (Table 1, Fig. 1), and the lower crustal rheology (25-35 km) is dry Maryland diabase (*B*(DMD)*; Mackwell *et al.* 1998), also with ϕ_{eff} = 15°. The strong lower crust is subducted and does not influence pro-side model evolution, although it extends as a 10-km layer along the base of the orogen to the S-point. Both model orogens therefore consist of thickened middle and upper crust, and their thermal evolution is mainly controlled by crustal heat production (A_1 = 2.0 μW/m^3, 0-20 km; A_2 = 0.75 μW/m^3, 20-35 km). Material flow in the models is tracked using contrasting colours for mid-crustal blocks (Fig. 2), which are initially 200 km wide and have identical material properties.

In both models, the effective viscosity is reduced linearly from its flow law value at 700°C to 10^{19} Pa.s at $T \geq 750$°C (Fig. 1; Beaumont *et al.* 2001). For convenience, we refer to this as 'melt weakening', because the effect is probably comparable to that produced by the presence of a small amount of *in situ* partial melt (e.g., van der Molen & Paterson 1979; Rosenberg & Handy in press). However, any other geological process producing a reduction in effective viscosity by a factor of about 10 over the same temperature range would have a similar effect in the model.

Exhumation in both models is controlled by surface denudation, which varies with time, distance, and local surface slope (Beaumont *et al.* 2004; Jamieson *et al.* 2004). The time- and space-dependent denudation functions, identical in models HT1 and HT111, are pre-defined (*f(t), g(x)*; Fig. 1, Table 1). Until 30 Ma there is no erosion; this is followed by a high erosion rate until 15 Ma and a gradually declining erosion rate until the end of the model (details in Fig. 10 of Jamieson *et al.* 2004). Slope-dependent surface denudation is focused on the pro-side flank of the orogenic plateau. The local surface slope is determined by the interaction of model tectonics with the imposed denudation functions, leading to slight differences in denudation patterns between the two models (Fig. 3, 4).

Crustal-scale model results

Tectonic and thermal results from model HT1 have been presented elsewhere (Beaumont *et al.* 2004; Jamieson *et al.* 2004) and only those features relevant to provenance are summarized here. Channel flow initiates at ca. 30 Ma and channel extrusion begins at ca. 15 Ma (Fig. 3). Initially the extruded channel is symmetrical, but a transition to an asymmetrical overthrust structure occurs between 15 and 6 Ma (Fig. 3) in response to detachment and outward flow of overlying upper crust (e.g. Medvedev & Beaumont this volume; Fig. 16d of Beaumont *et al.* 2004). "Tethyan" crust above the channel remains thick and strong enough to retain its coherence, and model HT1 does not develop domes between the suture and the erosion front (Fig. 3).

Model HT111 differs from model HT1 only in having a thin, weak layer (2.5 km, ϕ_{eff} = 2°) embedded in the upper crust. Until ca. 24 Ma the model evolves in a very similar manner to HT1 (Fig. 4), but the difference in upper crustal strength affects its subsequent tectonic evolution. The weak layer facilitates detachment and outward flow of the upper crust above the channel. Moreover, because the incoming foreland upper crust has the same material properties, i.e. it is weaker than equivalent crust in HT1, it offers less resistance to outward-flowing upper and middle orogenic crust. Consequently, the orogen in model HT111 propagates much further to the south than it does in HT1 (Fig. 3, 4), and for the denudation model used here the region between the suture and the orogenic front is much wider (ca. 370 km *vs.* ca. 200 km). Enhanced southward flow of orogenic crust in HT111 also enhances advection of isotherms with the channel, forming a thermal "lobe" that extends into the middle and upper crust (e.g., 6 Ma, Fig.

4). Incoming middle crust is cooler and stronger than the overlying channel, and takes some time to reach the 700°C melt-weakening threshold. As a result, the hot channel flow zone is forced up and over the cooler mid-crustal ramp, further destabilizing the weak upper crust, and forming a dome underlain by channel material. The first dome forms at ca.10 Ma, and is subsequently translated southward along with the channel ("egg-in-snake" effect) and extruded at the erosion front between 5 and 0 Ma. This process is similar to the creation and explusion of hot fold nappes in response to collision with a strong lower crustal indentor (Beaumont *et al.* this volume). Structures initially formed in a dome over a mid-crustal ramp may evolve into strongly flattened nappes during extrusion (Grujic *et al.* 2004). Continued convergence leads to the creation of a second dome, which at 0 Ma lies ca. 200 km north of the erosion front at a depth of ca. 10 km (Fig. 4). A more detailed analysis of the mechanics of dome formation in large hot orogens will be presented elsewhere (Beaumont *et al.* in prep).

In both models, outward flow of middle and upper plateau crust above the channel accompanies southward translation of the model suture (embedded in upper plateau crust) from its initial position directly over the S-point to a final position ca. 400 km south of the S-point (Fig. 3, 4). As a result, the entire model crust south of the surface exposure of the suture consists of "Indian" material. Both model orogens are also underlain at depth as far as the S-point by undeformed (10-km thick) "Indian" lower crust (Fig. 6).

The behaviour of upper and middle plateau crust in HT111 is affected by the embedded weak layer, leading to a significant difference in crustal structure between the two models north of the suture. In model HT1, the upper crustal layer immediately north of the suture thickens significantly during the early stages of convergence (Fig. 3,5), leading to necking of the underlying mid-crustal layer and its eventual detachment from strong "Asian" lower crust after ca. 24 Ma. By 0 Ma, "Indian" crust not only underlies the entire region between the erosion front and the suture, but extends beneath "Asian" upper and middle plateau crust for another 200 km to the north. In contrast, in model HT111, the weak upper plateau crust does not thicken significantly. "Asian" upper and middle crust remains coupled to "Asian" lower crust, and all are transported southward along with the suture above a thin (<20 km), highly attenuated zone of "Indian" crust. At the end of the model, the upper two-thirds of HT111 crust north of the suture consists of "Asian" material, whereas HT1 crust in the same region consists largely of "Indian" material. We do not regard the model predictions for deformation in the vicinity of the suture to be robust - for example, the properties of the suture zone in the Himalayan-Tibetan system probably differ significantly from the laterally homogeneous material properties assumed here. However, the results illustrate that the behaviour of the "Asian" crust is sensitive to subtle variations in model properties.

Provenance of GHS and LHS

In the Himalayan-Tibetan orogen south of the Indus-Tsangpo suture, the entire crust, including the GHS and LHS, is interpreted to consist of the deformed and metamorphosed continental margin of northern India (e.g. Myrow *et al*. 2003). The pre-Cambrian isotopic signature of the GHS ($\varepsilon_{Nd} < 20$, $T_{DM} < 2.0$ Ga, detrital zircons 500-1000 Ma) indicates that it is a Neoproterozoic to early Paleozoic Gondwanan succession, whereas the isotopically distinct LHS ($\varepsilon_{Nd} > 20$, $T_{DM} > 2.0$ Ga, detrital zircons 1600-2600 Ma) is inferred to represent a Paleo- to Mesoproterozoic sequence (e.g. Parrish & Hodges 1996; Hodges 2000; DeCelles *et al.*, 2000, 2004). Within the GHS, lithological units are laterally continuous along-strike for considerable

distances, and a consistent regional stratigraphy can be recognized through much of the orogen (Hodges 2000, and references therein).

In models HT1 and HT111, the entire region between the model suture and the orogenic foreland is occupied by "Indian" material (Fig. 5, 6). On a crustal scale, therefore, material distribution in the models is compatible with observations. The model "MCT" is the protolith boundary between outflowing ("GHS") and inflowing ("LHS") material. In model HT1, the offset across the "MCT" is ≥ 600 km (Jamieson *et al.* 2004), whereas in HT111, the missing section is ≥ 400 km when dome material is taken into account (Fig. 2). In both cases, "GHS" at the model surface is derived from distal "Indian" upper and middle crust originating ≤ 1000 km south of the model suture, whereas "LHS" material is derived mainly from proximal crust originating ≥ 1400 km south of the suture (Fig. 2, 7, 8).

At the end of model HT1, "GHS" material at the model surface, although strongly deformed, is largely derived from contiguous Indian middle crust (Fig. 5, 7), because it is mainly the upper part of the channel that is extruded between 6 and 0 Ma (Fig. 7, 8). Particle tracking indicates little or no mixing of diverse crustal elements in the exhumed region, so that units exposed at the surface could appear to retain a coherent "stratigraphy". However, in the model, this material has been strongly transposed and attenuated, so that the apparent stratigraphy is unlikely to reflect original depositional relationships. Furthermore, intense deformation and transposition at depth beneath the plateau flank (Fig. 3, 5) suggests that continued exhumation and extrusion would eventually expose a structurally and lithologically diverse tectono-metamorphic assemblage at the orogenic front.

The creation and extrusion of domes in model HT111 leads to a two-stage evolution for the "GHS". At 6 Ma, before the extruded dome has reached the surface, the geometry at the orogenic front is similar to that of HT1, with the strongly deformed "GHS" lying between the "MCT" and "STD" (Fig. 4, 6). However, the final stage of dome extrusion (5-0 Ma) strongly affects the geometry and distribution of material above the "MCT". The previously exhumed "GHS" becomes progressively shortened as it is overridden from the north. Because the early, structurally lower "GHS" and the later, structurally higher extruded dome both consist of high-grade material, it could be very difficult to distinguish between them in the field. Peak grade and age profiles from model HT111 (Jamieson, unpublished data) suggest that discontinuities in structure, metamorphism, and age should be detectable with sufficiently detailed observations. For example, it might be possible to recognize multiple thrust- and normal-sense structures bounding different high-grade "GHS" packages, and the "lower GHS" should have significantly older peak metamorphic and cooling ages than the "upper GHS". A more detailed discussion of the tectonic-metamorphic consequences of dome extrusion is presented elsewhere (Grujic *et al.* 2004, in prep).

At 6 Ma, material distribution in model HT111 "GHS" resembles that in model HT1 at 0 Ma, with originally contiguous crustal materials extruded as attenuated sheets between the "MCT" and "STD" (Fig. 5, 7). The "lower GHS" retains its lithological characteristics during the progressive shortening that accompanies dome extrusion (5-0 Ma), but material distribution within the extruded dome is more complex. The uppermost structural level within the dome consists of deformed "Tethyan" crust, which passes downward into highly deformed "Indian" middle crust overlying strongly attenuated channel material, both with "GHS" affinities. During the formation of domes, the channel is underplated at depth by material derived from the leading edge of the mid-crustal ramp (Fig. 6). Model HT111 therefore predicts that a transect through a deeply dissected dome should reveal a transition at depth from distal "GHS" protoliths into rocks

with more proximal crustal signatures. This transition, if it exists in nature, is unlikely to be exposed in any of the north Himalayan gneiss domes (see below), but its strongly deformed equivalent may be preserved in extruded domes that have reached the orogenic front.

Both models HT1 and HT111 predict that the "LHS" should be derived from proximal "Indian" crust that should be readily distinguishable from distal "GHS" protoliths. As noted above, this is consistent with observations from the Himalaya (e.g. Parrish & Hodges 1996; DeCelles *et al.* 2000). Furthermore, some general predictions can be made about the provenance of sediments eroded from the orogen after 30 Ma (onset of erosion in both models). Initially, the material being eroded consists entirely of "Tethyan" upper crust, but by 24 Ma "Indian" mid-crust is being exhumed at the orogenic front. The first material to be exposed originates ca. 1000 km south of the suture (Fig. 3, 4) and would probably have isotopic and detrital zircon signatures more akin to "GHS" than "LHS" lithologies. By 15 Ma, continued convergence and channel extrusion have juxtaposed distal "GHS" protoliths (above the "MCT") with more proximal "LHS" material (below the "MCT") at the erosion front, and this situation persists until the end of the model. Detrital zircon and isotopic data show significant changes in the provenance of Cretaceous to Miocene sedimentary rocks in the Lesser Himalaya (e.g. Najman & Garzanti 2000; DeCelles *et al.* 2004). Tertiary strata were deposited in the Himalayan foreland and became incorporated into the orogen as it propagated to the south; these rocks therefore preserve a record of the early unroofing history of the orogen. Eocene and older strata were derived from Tethyan source rocks, but Early Miocene strata record the influx of GHS detritus. Material with LHS signatures first appears in the Early to Middle Miocene, and both GHS and LHS detritus is present after that time. Within the spatial and temporal resolution of the models, results from HT1 and HT111 appear to be generally consistent with the Lesser Himalayan provenance data.

Provenance of gneiss domes and leucogranites

The north Himalayan gneiss domes, which lie in the Tibetan plateau south of the Indus-Tsangpo suture, are cored by gneisses resembling those exposed in the GHS (e.g. Wu *et al.* 1998; Zhang *et al.* 2004). These rocks exhibit condensed metamorphic sequences, are locally cut by leucogranites, and are separated from overlying lower grade rocks of the Tethyan Series by ductile shear zones and brittle normal faults (e.g. Lee *et al*. 2000, 2004). Petrological and isotopic studies of Miocene leucogranites in both the Himalaya and the gneiss domes suggest that they were derived by melting of GHS source rocks (e.g. Inger & Harris 1993; Patiño Douce & Harris 1998; Harrison *et al.* 1999; Zhang *et al.* 2004).

Material tracking in models HT1 and HT111 shows that the entire model crust south of the suture is made up of "Indian" material. Although channel flow has transported distal middle crust to the erosion front, the suture and its surrounding "Tethyan" crust have also been transported southward. Channel flow at depth has not yet carried "Asian" middle and lower crust significantly beyond the surface exposure of the suture. Both models therefore predict that leucogranites and gneiss domes located south of the suture should record "Indian" provenance. Furthermore, continuous transport of material into the orogen from the "Indian" side of the system provides a continuous supply of fertile source material for diachronous leucogranite generation. As noted above, model HT111 predicts that material within the north Himalayan gneiss domes should resemble the "GHS", although relatively more distal (shallower) and proximal (deeper) "Indian" crust are juxtaposed during dome formation (Fig. 5, 7). Model predictions for the region south of the Indus-Tsangpo suture are therefore compatible with each other and with observations from leucogranites and gneiss domes south of the suture.

The two models make different predictions, however, for plutons and gneisses formed north of the suture. In model HT1, "Indian" material makes up most of the crust for 200 km north of the suture, suggesting that granites and gneisses originating at depths greater than ca. 30 km should have "Indian" crustal signatures in this region, although mixed signatures could be produced by assimilation of upper crust. In model HT111, however, "Asian" middle and lower crust is transported southward along with overlying "Tethyan" material, so that crustally derived plutons and gneisses north of the suture should have dominantly "Asian" characteristics.

In addition to isotopic constraints on source rock characteristics, petrological and geochronological studies of Himalayan leucogranites provide P-T-t data that can be compared directly with model P-T-t paths. Many Himalayan leucogranites are interpreted to have formed at 20-25 Ma by dehydration melting of muscovite-bearing GHS protoliths at mid-crustal depths (e.g. Inger & Harris 1993; Patiño Douce & Harris 1998; Harrison *et al.* 1999). Early (ca. 40 Ma) fluid-present melting has been inferred in some places (e.g. Prince *et al.* 2001), and both melting and emplacement are locally inferred to have taken place at relatively low pressure (<5 kb; e.g. Visonà & Lombardo 2002). Plutons significantly older (≥ 30 Ma) and younger (≤15 Ma) than the typical Miocene range have also been reported from various parts of the orogen (e.g. Edwards & Harrison 1997; Zhang *et al.* 2004).

In models HT1 and HT111, P-T-t paths from the lower "GHS" pass through the medium-pressure muscovite dehydration melting field between 30 and 15 Ma (Fig. 9), demonstrating that both models are capable of generating the necessary P-T conditions at the right time. P-T-t paths from the upper "GHS" (G2, D3) lie mainly within the fluid-present melting field and some (e.g. G1, model HT1) pass through this field before 40 Ma (Fig. 9a). Both models can therefore account for fluid-present melting between ca. 45 Ma and 6 Ma. None of the "GHS" P-T-t paths from model HT1 pass through the low-pressure andalusite + melt field; this model therefore cannot explain andalusite-bearing leucogranites such as the Makalu.pluton (Visonà & Lombardo 2002). In contrast, dome formation and extrusion in model HT111 leads to isothermal decompression; the resulting "GHS" P-T-t paths stay in the melting field beyond 15 Ma, crossing into the andalusite + melt field after 12 Ma (Fig. 9b). Models of this type provide an explanation for both low-pressure leucogranites and the generation of post-15 Ma plutons. P-T-t paths from the second (buried) dome in HT111 (Jamieson, unpublished data) indicate that the conditions necessary for medium-pressure leucogranite generation are reached in dome cores by ca. 24 Ma. This is consistent with relatively young intrusion ages reported from some north Himalayan gneiss domes (e.g. Wu *et al.* 1998; Zhang *et al.* 2004).

Discussion and conclusions

Within the temporal and spatial resolution of the models, material tracking in HT1 and HT111 suggests that channel flow models are consistent with provenance data from the Himalaya and southern Tibet. In particular, the models predict that channel flow has not yet transported "Asian" crust south of the model suture, consistent with Indian crustal signatures from a variety of metamorphic, igneous, and sedimentary rocks in the southern part of the orogen. In the lower model orogenic crust, strongly deformed materials from diverse "Indian" sources have been juxtaposed (Fig. 5, 6). In both models, however, material in the exhumed region corresponding to the "GHS" is derived mainly from originally contiguous protoliths and could appear to retain a coherent stratigraphy.

An important implication of the model results presented here and elsewhere (Beaumont *et al.* 2004; Jamieson *et al.* 2004) is that channel flow and many other orogenic processes are

inherently diachronous, involving substantial lateral transport of both heat and material. Material emerging today at the orogenic front has passed through several different thermal-tectonic regimes during its transit through the orogen; those regimes may persist today in the interior of the orogen. For example, dome formation and extrusion in model HT111 is continuous; as one dome is extruded at the orogenic front, another forms above the mid-crustal ramp. Convergence in the Himalayan-Tibetan system continuously brings new material into the orogen. Incoming material may eventually become involved in channel flow and re-emerge at the orogenic front, but most of the material that enters the orogen remains deeply buried. The models suggest that the distinctive GHS and LHS provenance signatures observed today do not represent the composition of the orogenic crust as a whole, but only that portion that has recently reached the surface.

Models HT1 and HT111 were chosen to illustrate contrasting tectonic styles in the region between the Indus-Tsangpo suture and the Himalayan front. Differences in tectonic style, including the width of the orogen, generation and extrusion of domes, and the behaviour of "Asian" crust, are produced by a small difference in the mechanical properties of model "Tethyan" crust. Previous work (Beaumont *et al.* 2004; Jamieson *et al.* 2004) showed that model HT1 is consistent with metamorphic and tectonic data from the central part of the orogen, and the present study shows that it is also compatible with a range of provenance data. Model HT111, although not yet subjected to the same degree of scrutiny, is equally compatible with the provenance data summarized here. In addition, HT111 can explain some observations (e.g. domes) not accounted for by HT1. We interpret models HT1 and HT111 to represent members in a spectrum of channel flow model styles that could be applied to different parts of the Himalayan-Tibetan system and/or to different stages in its evolution. Furthermore, the homogeneous channel flow mode represented by models HT1 and HT111 is only one of several possible flow modes in large hot orogens (Beaumont *et al.* this volume). It is conceivable that other flow modes (heterogeneous channel flow, hot fold nappes) could have operated in some parts of the Himalayan-Tibetan system at various times.

We conclude that channel flow models in general provide a reasonable first-order explanation for the thermal-tectonic and lithological evolution of the Himalaya and southern Tibet. However, more than one model style may be compatible with the observations and no single model is capable of explaining all the features of the orogen. The models lack the spatial-temporal resolution required for transect-specific comparisons, and are sensitive to subtle variations in input parameters that are already greatly simplified by comparison with nature. We therefore caution against using detailed transect-specific data to test the models; observations that can be integrated on a regional, crustal, or lithospheric scale provide a better basis for comparison.

Acknowledgements: This work was funded by NSERC Discovery Grants to Jamieson, Beaumont, and Grujic. Beaumont acknowledges support from the Canada Research Chairs programme and an IBM Shared University Research grant, and Grujic from the Canadian Institute for Advanced Research. The ALE numerical model was developed by Philippe Fullsack, Dalhousie University, and material tracking was implemented with the assistance of Sergei Medvedev, Freie Universität, Berlin. The work has benefited from discussions with, and constructive criticism by, a number of Himalayan-Tibetan researchers, including Peter DeCelles, Nigel Harris, Kip Hodges, Linc Hollister, Yani Najman, and especially the late Doug Nelson.

We are grateful to the conference organizers for providing a stimulating environment in which to present and discuss this work.

References

Beaumont, C., Jamieson, R.A., Nguyen, M.H. & Lee, B. 2001. Himalayan tectonics explained by extrusion of a low-viscosity channel coupled to focused surface denudation. *Nature*, **414**, 738-742.

Beaumont, C., Jamieson, R.A., Nguyen, M.H. & Medvedev, S. 2004. Crustal channel flows: 1. Numerical models with applications to the tectonics of the Himalayan-Tibetan orogen. *Journal of Geophysical Research* **109**, B06406, doi:10.1029/2003JB002809.

Beaumont, C., Nguyen, M.H., Jamieson, R.A. & Lee, B. Crustal flow modes in large hot orogens. *Geological Society of London* (this volume, submitted).

Davidson, C., Grujic, D., Hollister, L.S. & Schmid, S.M. 1997. Metamorphic reactions related to decompression and synkinematic intrusion of leucogranite, High Himalayan Crystallines, Bhutan. *Journal of Metamorphic Geology*, **15**, 593-612.

DeCelles, P.G., Gehrels, G.E., Najman, Y., Martin, A.J., Carter, A. and Garzanti, E. 2004. Detrital geochronology and geochemistry of Cretaceous-Early Miocene strata of Nepal: implications for timing and diachroneity of initial Himalayan orogenesis. *Earth and Planetary Science Letters* **227**, 313-330.

DeCelles, P.G., Gehrels, G.E., Quade, J., LaReau, B. & Spurlin, M. 2000. Tectonic implications of U-Pb zircon ages of the Himalayan orogenic belt in Nepal. *Science*, **288**, 497-499.

Edwards, M.A. & Harrison, T.M. 1997. When did the roof collapse? Late Miocene north-south extension in the High Himalaya revealed by Th-Pb monazite dating of the Khula Kangri granite. *Geology* **25**, 543-546.

Fullsack, P., 1995. An arbitrary Lagrangian-Eulerian formulation for creeping flows and its application in tectonic models. *Geophysical Journal International,* **120***,* 1-23.

Gleason, G.C. & Tullis, J. 1995. A flow law for dislocation creep of quartz aggregates determined with the molten salt cell. *Tectonophysics*, **247**, 1-23.

Grujic, D., Beaumont, C., Jamieson, R.A. & Nguyen, M.H. 2004. Extruded domes in the Greater Himalayan Sequence: Model predictions and possible examples. *Geological Society of London,* Channel Flow Conference, London, December 2004 (abstract volume)

Harrison, T.M., Grove, M., McKeegan, K.D., Coath, C.D., Lovera, O.M. & LeFort, P. 1999. Origin and episodic emplacement of the Manaslu intrusive complex, central Himalaya. *Journal of Petrology,* **40**, 3-19.

Hodges, K.V. 2000. Tectonics of the Himalaya and southern Tibet from two perspectives. *Geological Society of America Bulletin*, **112**, 324-350.

Holdaway, M.J. 1971. Stability of andalusite and the aluminosilicate phase diagram. *American Journal of Science*, **271**, 97-131.

Gardien, V., Thompson, A.B. & Ulmer, P. 2000. Melting of biotite+plagioclase+quartz gneisses: The role of H_2O in the stability of amphibole. *Journal of Petrology* **41**, 651-666.

Inger, S. & Harris, N.B.W. 1993. Geochemical constraints on leucogranite magmatism in the Langtang Valley, Nepal Himalaya. *Journal of Petrology* **34**, 345-368.

Jamieson, R.A., Beaumont, C., Medvedev, S. & Nguyen, M.H. 2004. Crustal channel flows: 2. Numerical models with implications for metamorphism in the Himalayan-Tibetan orogen. *Journal of Geophysical Research* **109**, B06406, doi:10.1029/2003JB002811.

Lee, J., Hacker, B.R., Dinklage, W.S., Wang, Y., Gans, P., Calvert, A., Wan, J.L., Chen, W., Blythe, A.E., & McLelland, W. 2000. Evolution of the Kangmar Dome, southern Tibet: Structural, petrologic, and thermochronologic constraints. *Tectonics*, **19**, 872-895.

Lee, J., Hacker, B. & Wang, Y. 2004. Evolution of the north Himalayan gneiss domes: structural and metamorphic studies in Mabja Dome, southern Tibet. *Journal of Structural Geology,* **26**, 2297-2316.

Mackwell, S.J., Zimmerman, M.E. & Kohlstedt, D.L. 1998. High-temperature deformation of dry diabase with application to tectonics on Venus. *Journal of Geophysical Research*, **103**, 975-984.

Medvedev, S. & Beaumont, C. Growth of continental plateaus by crustal channel injection: Constraints and thermo-mechanical consistency. *Geological Society of London* (this volume, submitted).

Myrow, P.M., Hughes, N.C., Paulsen, T.S., Williams, I.S., Parcha, S.K., Thompson, K.R., Bowring, S.A., Peng, S-C. & Ahluwalia, A.D. 2003. Integrated tectonostratigraphic analysis of the Himalaya and implications for its tectonic reconstruction, *Earth and Planetary Science Letters,* **212,** 433-441.

Najman, Y. & Garzanti, E. 2000. Reconstructing early Himalayan tectonic evolution and paleogeography from Tertary foreland basin sediments, northern India. *Geological Society of America Bulletin*, **112**, 435-449.

Parrish, R.R. & Hodges, K.V. 1996. Isotopic constraints on the age and provenance of the Lesser and Greater Himalayan sequences, Nepalese Himalaya. *Geological Society of America Bulletin*, **108**, 904-911.

Patiño Douce, A.E. & Harris, N. 1998. Experimental constraints on Himalayan anatexis. *Journal of Petrology,* **39**, 689-710.

Pattison, D.R.M. 1992. Stability of andalusite and sillimanite and the Al_2SiO_5 triple point: constraints from the Ballachulish aureole. *Journal of Geology,* **100**, 423-446.

Peto, P.1976. An experimental investigation of melting relations involving muscovite and paragonite in the silica-saturated portion of the system K_2O-Na_2O-Al_2O_3-SiO_2-H_2O to 15 kb total pressure. *Progress in Experimental Petrology*, **3**, 41-45.

Prince, C., Harris, N. & Vance, D. 2001. Fluid-enhanced melting during prograde metamorphism. *Journal of the Geological Society, London*, **158**, 233-241.

Rosenberg, C.L. & Handy, M.R. in press. Experimental deformation of partially melted granite revisited: Implications for the continental crust. *Journal of Metamorphic Geology*

Stevens, G. & Clemens, J.D. (1993). Fluid-absent melting and the roles of fluids in the lithosphere: A slanted summary? *Chemical Geology,* **108**, 1-17

van der Molen, I. & Paterson, M.S. (1979) Experimental deformation of partially-melted granite. *Contributions to Mineralogy and Petrology* **70**, 299-318.

Visonà, D. & Lombardo, B. 2002. Two-mica and tourmaline leucogranites from the Everest-Makalu region (Nepal-Tibet). Himalayan leucogranite genesis by isobaric heating? *Lithos* **62**, 125-150.

Wu, C., Nelson, K.D., Wortman, G., Samson, S.D., Yue, Y., Li., J., Kidd, W.S.F. & Edwards, M.A. 1998. Yadong cross structure and the South Tibetan Detachment in the east central Himalaya (89°-90°E). *Tectonics*, **17**, 28-45.

Zhang, H., Harris, N., Parrish, R., Kelley, S., Zhang, L., Rogers, N., Argles, T. & King, J. 2004. Causes and consequences of protracted melting of the mid-crust exposed in the North Himalayan antiform. *Earth and Planetary Science Letters* **228**, 195-212.

Figure Captions

NB: Where necessary, figures will be redesigned and/or relabeled to fit *Geological Society of London* specifications and format. Some colour mismatch (eg Fig.8) has occurred during processing; these problems will be corrected at revision stage.
Results from similar models and animations can be viewed at http://geodynam.ocean.dal.ca

Figure 1. Model parameters and initial conditions; a full list of parameters is presented in Table 1. a) Mechanical model showing initial distribution of crustal layers. b) Thermal model showing temperature (isotherms) and velocity fields (short lines); the model is started in conductive steady-state. c) Mechanical and thermal properties of crustal layers. Model HT111 differs only from HT1 in having a thin weak layer (ϕ_{eff} = 2°, 2.5 km) embedded in the upper crust (column at far right). Further details in text and Jamieson *et al.* (2004).

Figure 2. Material distribution at the start of the model (54 Ma). The colour blocks in the mid-crustal layer are used for tracking purposes only; there is no lateral difference in material properties. The initial width of each colour block is 200 km. Labeled symbols show the initial positions of selected tracked points in model HT1 (squares) and HT111 (circles). "GHS" P-T-t paths from tracked points G1, G2 (model HT1), and D1, D2, D3 (model HT111) are shown in Figure 9; "LHS" points (L3, LD) are shown for illustration only; P-T-t path for L3 was presented by Jamieson *et al.* (2004).

Figure 3. Tectonic and thermal evolution, model HT1, for selected time steps; equivalent results for other times are presented by Beaumont *et al.* (2004) and Jamieson *et al.* (2004). All times are given in Ma (millions of years before end of model) to facilitate comparison with observations. Δx = total amount of convergence (km). The upper panel in each pair shows a deformed passive marker grid and distribution of mid-crustal materials (coloured blocks) whose initial distribution is shown in Figure 2. The graph above the model surface shows the spatial distribution of surface denudation for each time step; the vertical axis shows erosion rate (scale bar = 10 mm/y). Maximum erosion rate (e_{max}) for each time step is also noted, along with provenance data summarized from DeCelles *et al.* (2004). The lower panel in each pair shows the corresponding temperature field (700°C isotherm = melt-weakening threshold), velocity field (short black lines) and distribution of heat-producing material (shaded region corresponds to material A_1, Table 1, Fig. 1).

Figure 4. Tectonic and thermal evolution, model HT1. Details as in Figure 3. At 24 Ma the model is very similar to HT1, but note formation and expulsion of domes following 15 Ma.

Figure 5. Crustal-scale material distribution, model HT1. Initial distribution of colour blocks and tracked points (squares) shown in Fig. 2. Details of material distribution at orogenic front at 6 Ma and 0 Ma (boxes) shown in Fig. 7. Grey zone at base of model shows extent of Indian lowermost crustal layer (10 km thick, subducted and therefore not deformed in model). Orogenic crust south of suture consists of "Indian" material, which also occupies most of the crust for ca. 200 km north of the suture.

Figure 6. Crustal-scale material distribution. model HT111. Initial distribution of colour blocks and tracked points (circles) shown in Fig. 2. Details of material distribution at orogenic front at 6 Ma and 0 Ma (boxes) shown in Fig. 8. Domes formed at 15 Ma consist of "GHS" material, underplated at depth by material derived from the leading edge of "Indian" mid-crustal ramp. Note contrast in distribution of "Asian" crust north of the suture compared to HT1 (Fig. 6).

Figure 7. Distribution of material points in the vicinity of the orogenic front, model HT1. 6 Ma and 0 Ma panels (48 and 54 million years, respectively, after model start) chosen to bracket

likely range of times since India-Asia collision (e.g. Hodges 2000; Myrow *et al.* 2003; DeCelles *et al.* 2004). Each coloured disk corresponds to a Lagrangian point tracked by the model. Initial distribution of colour blocks and tracked points (circles) shown in Fig. 2. Note that exhumed "GHS" corresponds mainly to the upper part of the channel flow zone; material originates from contiguous crustal domains and is not mixed significantly with "exotic" material during channel flow and extrusion.

Figure 8. Distribution of material points in the vicinity of the orogenic front, model HT111. Initial distribution of colour blocks and tracked points (squares) shown in Fig. 2. "GHS" material distribution at 6 Ma resembles that in HT1 at 0 Ma, but subsequent dome extrusion broadens the high-grade region and juxtaposes the more diverse dome material against the previously extruded "GHS".
NB: Colour difference in upper crustal layer (pale blue) between upper and lower panels is an artifact of processing. This will be corrected at revision stage.

Figure 9. P-T-t paths for selected "GHS" points in model HT1 (a) and model HT111 (b) compared with data relevant to generation of Himalayan leucogranites. Positions of tracked points at various times shown in Figs. 2, 5, 6, 7, 8. Other P-T-t paths from model HT1 presented by Jamieson *et al.* (2004). Alternate Al_2SiO_5 triple-point positions from Holdaway (1971; H71) and Pattison (1992; P92). Melting ranges and dehydration reactions from Peto (1976), Stevens & Clemens (1993), Patiño Douce & Harris (1998), and Gardien *et al.* (2000). P-T data from Davidson *et al*. (1997; Bhutan) and Visonà & Lombardo (2002; Makalu). P-T-t paths from both models cross the muscovite dehydration melting field between 30 and 15 Ma, and therefore predict leucogranite generation at the observed times. Isothermal decompression in model HT111 (D1, D2) results from dome creation and expulsion; P-T-t paths pass through the andalusite + melt stability field after 12 Ma.

Table 1. Parameters used in models HT1 and HT111 (see also Figure 1). Model HT111 differs from HT1 only in having a weak ($\phi_{eff} = 2°$) layer embedded in the upper crust (details below).

Parameter	**Meaning**	**Value(s)**
a) Mechanical parameters		
V_P	pro-side (convergence) velocity	5 cm/y
V_R	retro-side velocity	0 cm/y
V_S	S-point velocity (subduction advance)	2.5 cm/y
θ	subduction dip angle	20°
D	flexural rigidity (isostasy model)	10^{22} Nm
ρ_{crust}	crustal density	2700 kg/m^3
ρ_{mantle}	mantle density	3300 kg/m^3
ϕ_{eff}	effective internal angle of friction	
HT1:	upper crust	5° (0-10 km)
HT111:	upper crust	5° (0-4.5 & 7-10 km) 2° (4.5-7 km)
HT1 and HT111:	middle and lower crust	15° (10-35 km)
$\eta_{eff}^{v} = B^* \cdot (\dot{I}_2^{/})^{(1-n)/2n} \cdot \exp[Q/nRT_K]$	general equation for effective viscosity	
$\dot{I}_2^{/}$	second invariant of strain rate tensor	1/s
R	gas constant	8.314 J/mol°K
T_K	absolute temperature	°K
B(WQ)* (0-10 km)	wet Black Hills quartzite flow law (after Gleason & Tullis, 1995)	$n = 4.0$ $B^* = 2.92 \times 10^6$ Pa.s$^{1/4}$ $Q = 223$ kJ/mol
B(WQx5)* (10-25 km)	modified wet Black Hills quartzite flow law	$B^* = B^*(WQ) \times 5$ n, Q as above
B(DMD)* (25-35 km)	dry Maryland diabase flow law (after Mackwell *et al.* 1998)	$n = 4.7$ $Q = 485$ kJ/mol $B^* = 1.91 \times 10^5$ Pa.s$^{1/4.7}$
'melt weakening' (*B*(WQ)* and *B*(WQx5)* only)	linear reduction in effective viscosity over T range 700-750°C	η_{700} = flow law value $\eta_{750} = 10^{19}$ Pa.s
b) Thermal parameters		
$\rho C_p(\partial T/\partial t + \underline{v} \bullet \nabla T) = K\nabla^2 T + A$	heat balance equation	
C_P	heat capacity	750 m^2/ºKs^2
K	thermal conductivity	2.00 W/mºK
κ	thermal diffusivity ($\kappa = K/\rho C_p$, where $\rho C_p = 2 \times 10^6$)	1.0 x 10^{-6} m^2/s
T_a	temperature at lithosphere/ asthenosphere boundary	1350ºC
q_m	basal mantle heat flux	20 mW/m^2
q_s	initial surface heat flux	71.25 mW/m^2
A_1 (0-20 km)	upper crustal heat production	2.0 μW/m^3
A_2 (20-35 km)	lower crustal heat production	0.75 μW/m^3
T_{Moho}	initial temperature at Moho	704°C

Table 1 *(continued)*

c) Surface denudation

slope x *f(t)* x *g(x)*	denudation model	
slope	local surface slope (pro-flank of plateau)	
f(t)	time function	0.107 m/y for *t* = 30-15 Ma declining for *t* > 15 Ma
g(x)	spatial (climate) function	0 → 1 (dry → wet)

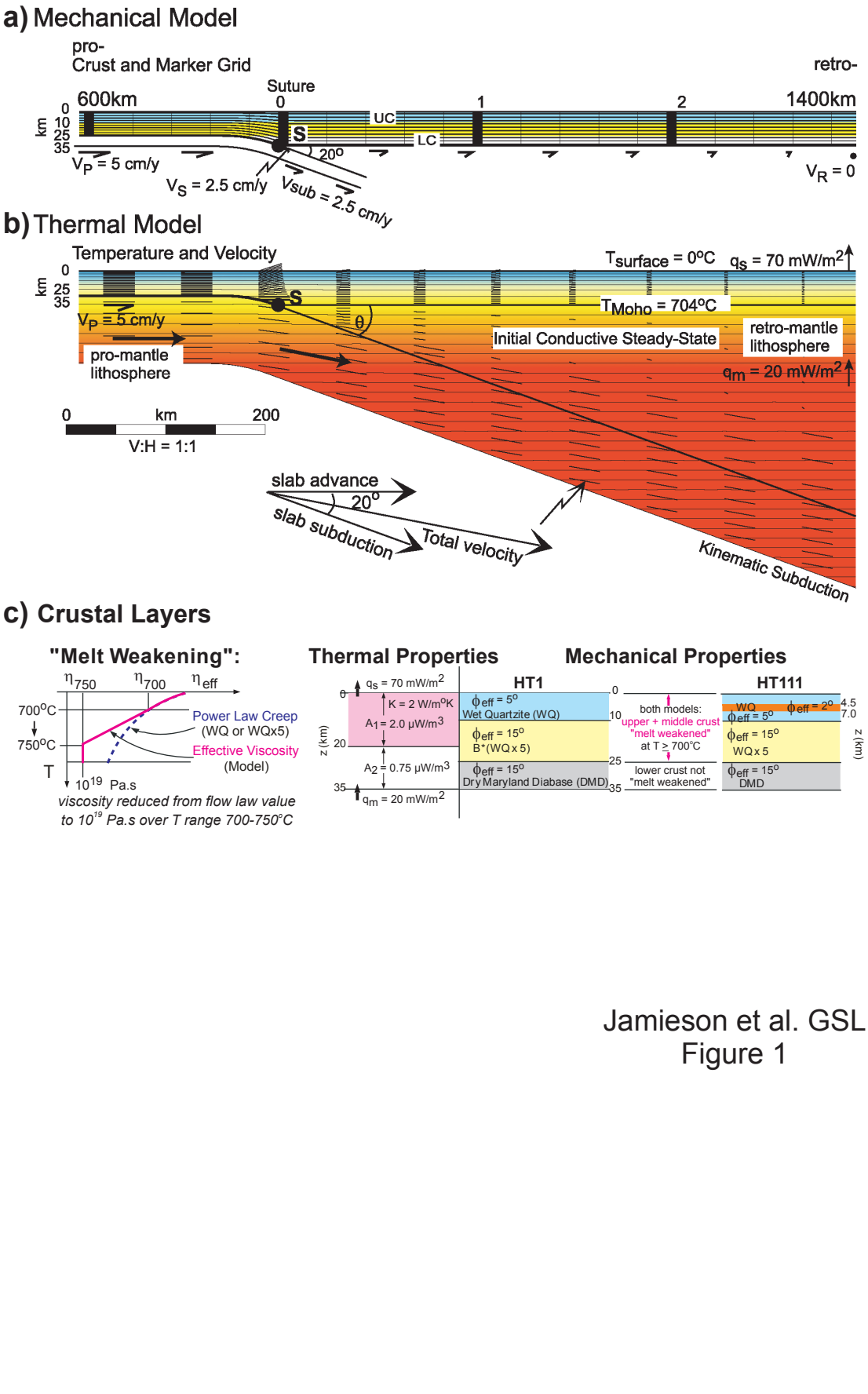

Jamieson et al. GSL
Figure 1

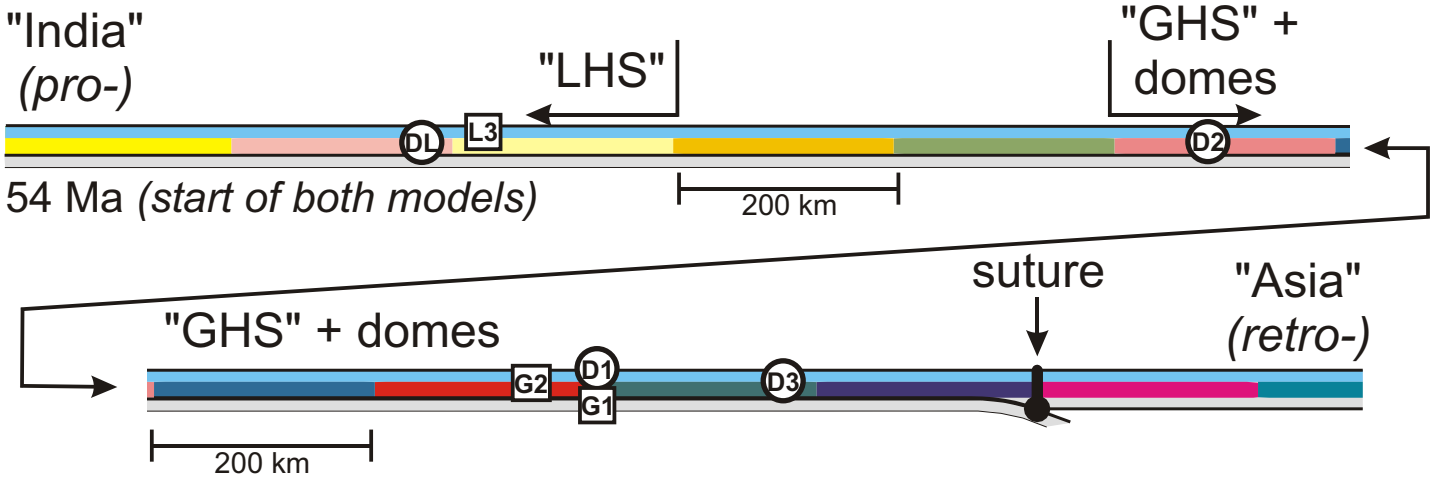

G1 G2 L3 Initial positions of tracked points, Model HT1

D1 D2 D3 DL Initial positions of tracked points, Model HT111

Jamieson et al. GSL
Figure 2

Model HT1

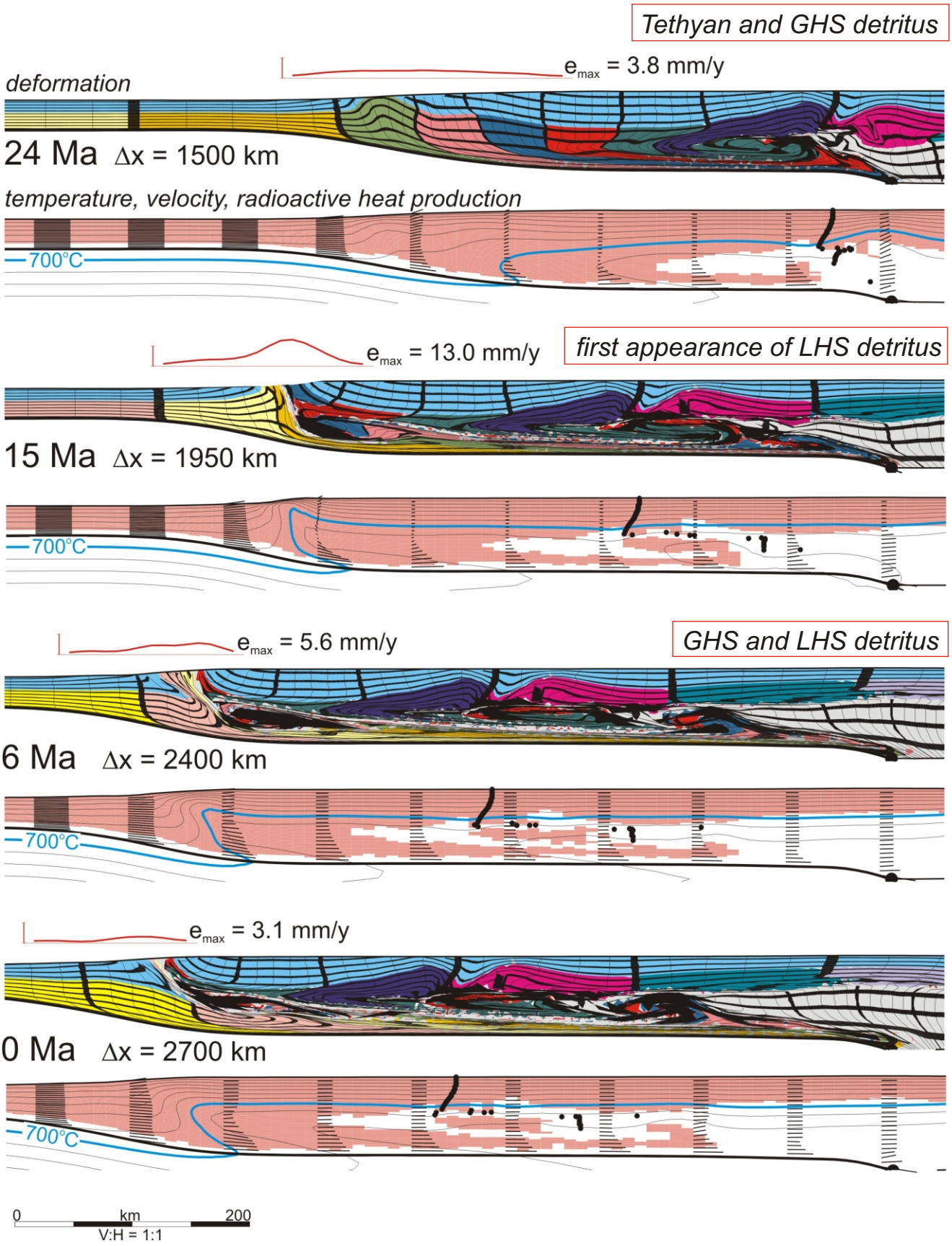

Jamieson et al. GSL
Figure 3

Model HT111

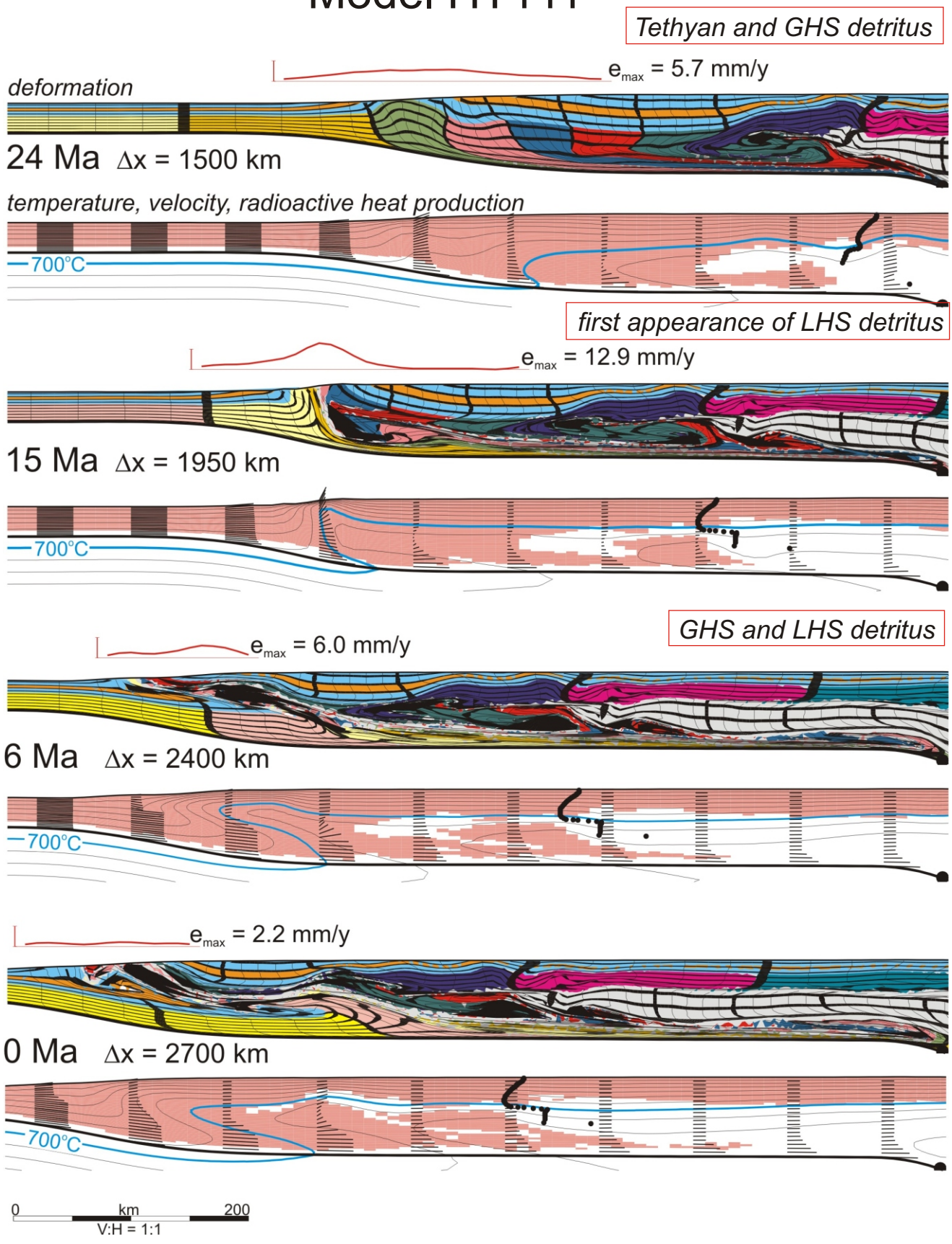

Jamieson et al. GSL
Figure 4

Model HT1

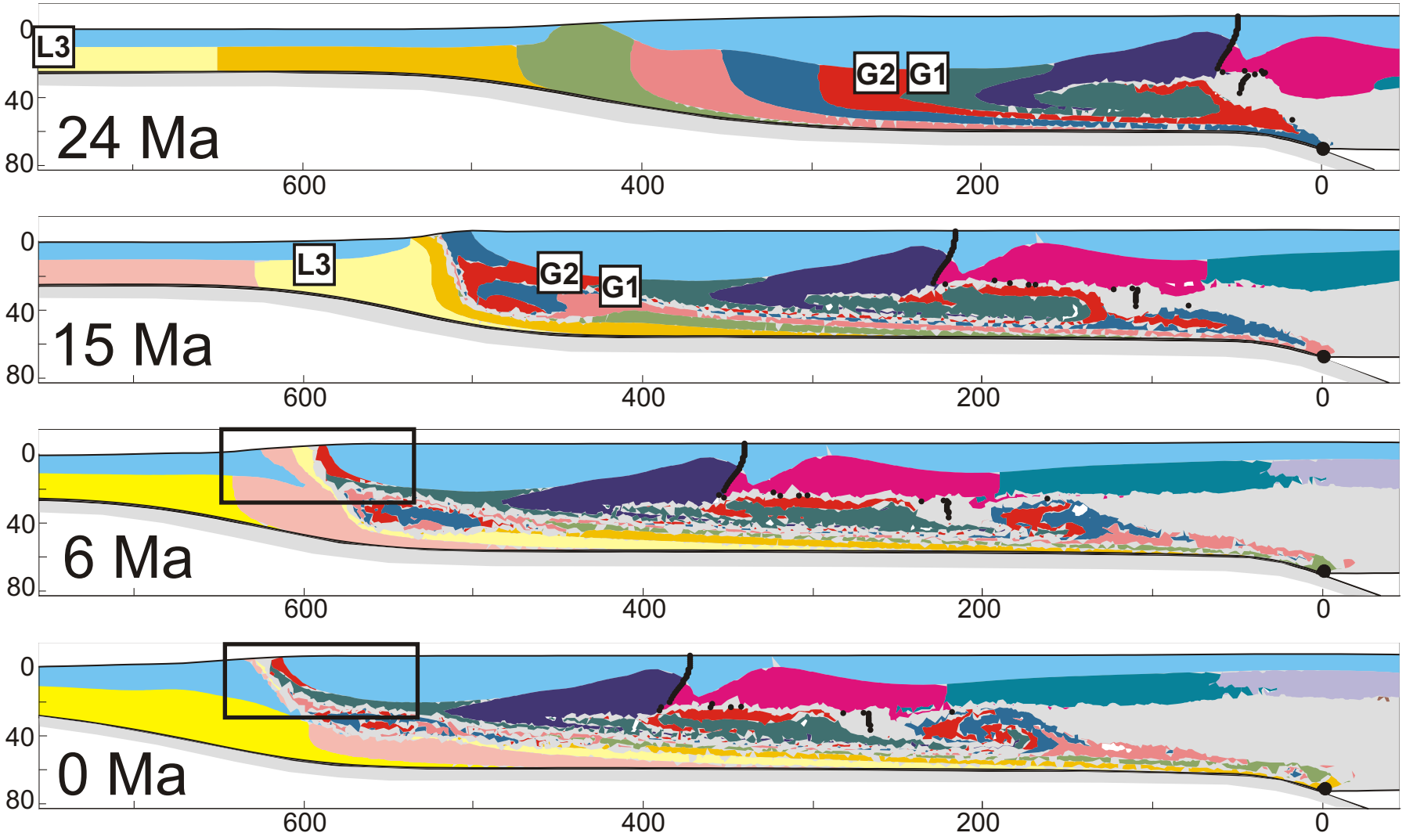

Jamieson et al. GSL
Figure 5

Model HT111

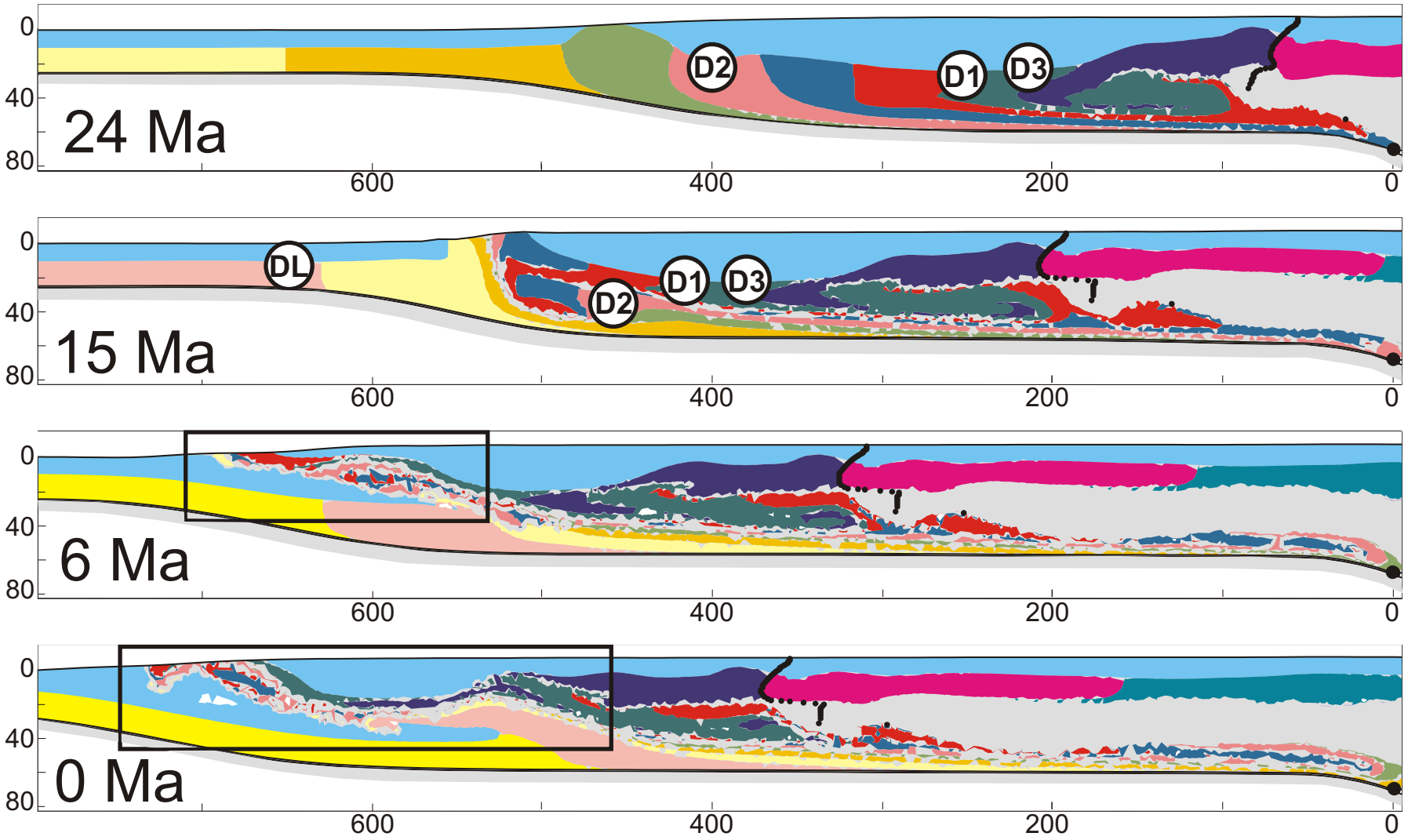

Jamieson et al. GSL
Figure 6

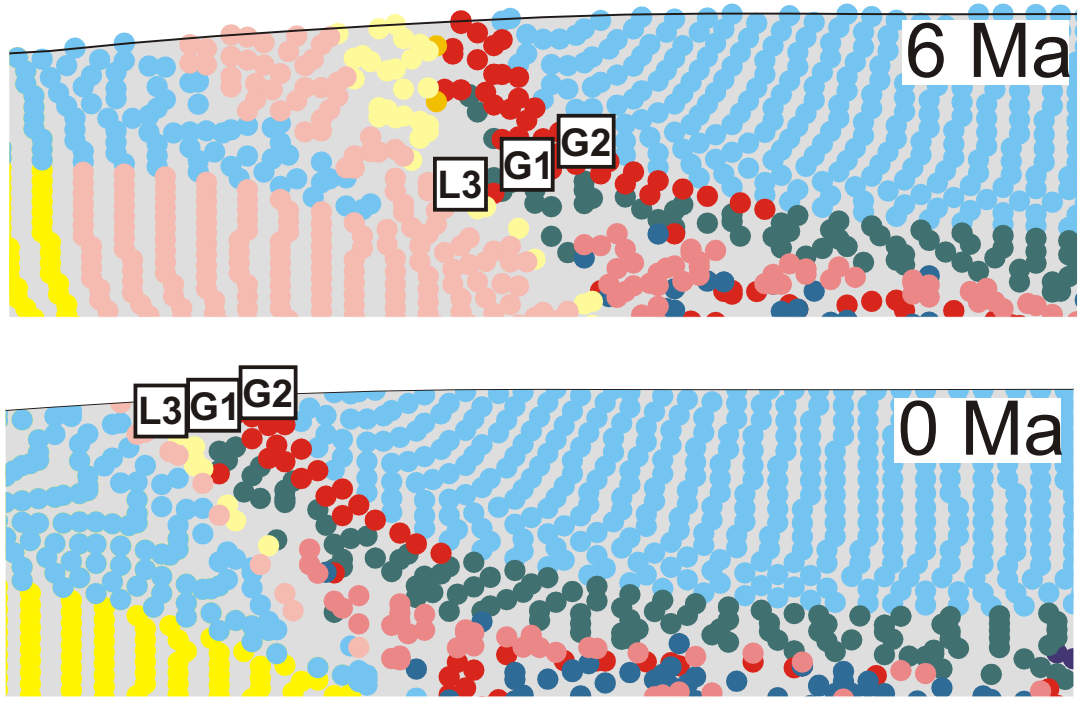

Model HT1

0 km 50

V:H = 1:1

Jamieson et al. GSL
Figure 7

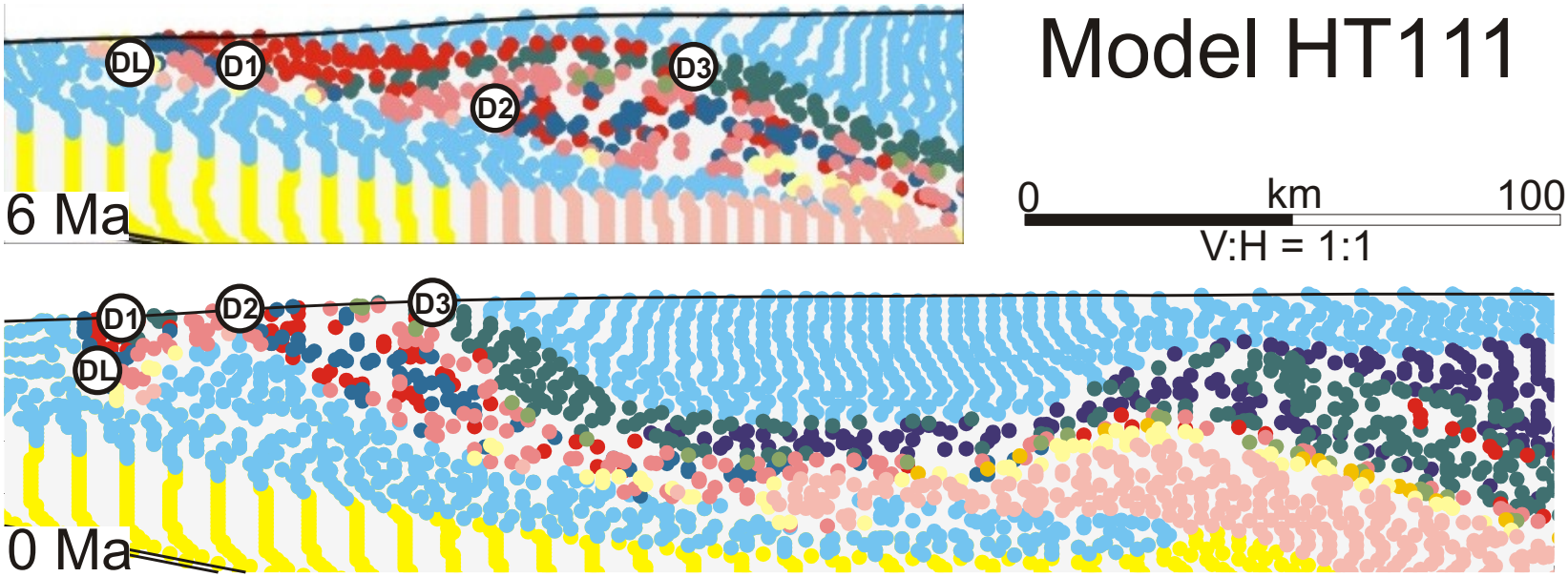

Jamieson et al. GSL
Figure 8

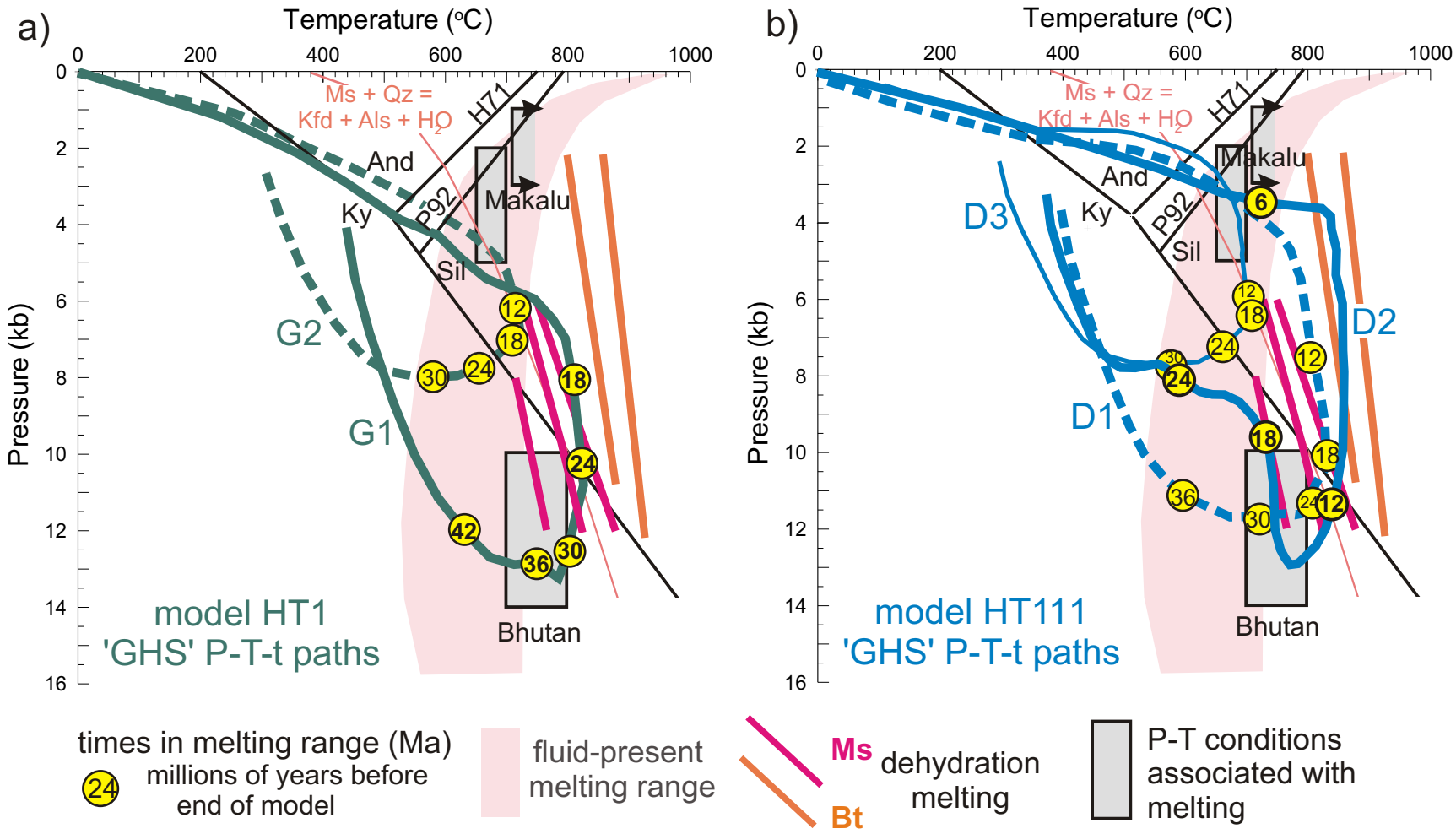

Jamieson et al. GSL
Figure 9